ASME Journal of Turbomachinery
Online journal at:
https://asmedigitalcollection.asme.org/turbomachinery

Transonic Linear Cascade Demonstration of Acoustic Flow Control on High Work and Lift Turbines

Acar Celik
Technion—Israel Institute of Technology,
Haifa 32000, Israel
e-mail: acar.celik@campus.technion.ac.il

Abhijit Mitra
Technion—Israel Institute of Technology,
Haifa 32000, Israel
e-mail: abhijitmitra@campus.technion.ac.il

John Clark
Air Force Research Laboratory,
1950 Fifth Street,
Wright Patterson AFB, OH 45433
e-mail: john.clark.38@us.af.mil

Beni Cukurel[1]
Technion—Israel Institute of Technology,
Haifa 32000, Israel
e-mail: beni@cukurel.org

The study explores acoustic flow control in high-lift, high-work turbine blades (L3FHW and L4FHW) tested in a transonic linear cascade facility to tackle flows with open separations at low Reynolds numbers caused by high adverse pressure gradients. Acoustic excitation aims to focus on frequencies associated with the Kelvin–Helmholtz instability, which scales with the 3/2 power of the exit Mach number. Two different acoustic sources were utilized: a siren disk and a passive perforated tailboard, which functioned as a Helmholtz resonator. Experiments across various Mach numbers, supported by Schlieren imaging and static pressure measurements. Key findings demonstrate that siren disk excitation increased peak suction pressure by up to 60%, while reducing the angle of the separated shear layer by 10 deg. The tailboard excitation yielded a similar reduction of up to 11 deg in the shear layer angle, albeit with modest improvements in pressure recovery near the trailing edge. Spectral analysis showed enhanced vortical coherence under excitation, with energy concentrating at target frequencies. Numerical simulations indicated up to 40% variation in peak suction pressure along the blade span due to end-wall vortices, suggesting secondary flows influencing the efficacy of flow control on midspan pressure distribution. Acoustic excitation demonstrated the ability to mitigate the adverse effects of end-wall vortices on pressure recovery. These findings highlight the potential of acoustic flow control to improve aerodynamic performance while underscoring the need to address secondary flow effects and integration challenges in advanced turbine designs.
[DOI: 10.1115/1.4069491]

Keywords: boundary layer development, fluid dynamics and heat transfer phenomena in compressor and turbine components of gas turbine engines, measurement techniques, turbine blade and measurement advancements, turbomachinery blading design

1 Introduction

1.1 Acoustic Flow Control. Early research on using acoustic actuation for flow control aimed to improve airfoil performance by deferring flow separation and enhancing turbulent mixing near the wall at intermediate frequencies, while reducing skin friction by suppressing turbulence at very high frequencies [1]. This approach significantly enhanced the performance, increasing lift by up to 50% and similarly reducing drag, especially in cases where there is separation or skin-friction losses are dominant [2]. The effectiveness of acoustic excitation relies on the wave's amplitude and frequency, which differ according to the body's geometry and operating Reynolds number [3].

Identifying the optimal frequency for specific applications remains an ongoing research focus. Studies from the 1980s found that targeting frequencies related to the inviscid instability of separated shear layers yielded the best flow response. Specifically, the optimal Strouhal numbers scaled with the square root of the Reynolds number, matching the Kelvin–Helmholtz (KH) mode scaling [4]. This first evidence led researchers to believe that acoustic waves directly excite the KH mode at the separation point [5,6]. However, there are two additional theories that were proposed as mechanisms of acoustic control: indirect feedback via the separation bubble [7–9] and indirect control of the KH instability through upstream wall modes [10–13]. Nevertheless, the theory of direct actuation raises theoretical concerns, suggesting that in incompressible flows, planar acoustic waves may not directly influence spanwise vorticity in wall-free shear layers without the involvement of viscous diffusive effects from a nearby wall [14]. Subsequently, the last theory was verified by Ref. [13], which demonstrated that the viscous wall mode organizes vorticity upstream of the separation point, with spatio-temporal analysis indicating this mode as the primary cause for changes in the separating shear layer and separation dynamics.

---

[1] Corresponding author.

Contributed by the International Gas Turbine Institute (IGTI) of ASME for publication in the JOURNAL OF TURBOMACHINERY. Manuscript received June 23, 2025; final manuscript received July 22, 2025; published online September 1, 2025. Assoc. Editor: David G. Bogard.

1.2 Flow Control Applications on Turbine Blades. Flow control over turbine blades could potentially become a crucial aspect of future jet engine design if it is aimed at improving efficiency while increasing the work on highly loaded blades. This complex field involves various techniques to manipulate the flow of air and other gases over the turbine blades, which can significantly impact the engine's operation [15]. Flow control strategies are essential in addressing issues such as boundary layer separation. These methods can be broadly categorized into passive and active methods. Passive flow control involves modifications to the blade geometry or surface properties to influence the flow without external energy input. Some applications of passive control on turbine blades are riblets [16], dimples [17], and surface roughness [18–20]. On the other hand, active flow control requires external energy to manipulate the flow. Several active control methods are applied to turbines, specifically synthetic jets [21–24], vortex generator jets [17], and plasma actuators [25]. Acoustic flow control, on the other hand, can be classified as either active or passive flow control, depending on the origin of the unsteadiness driving the mechanism. Among the various active control techniques, acoustic forcing offers the unique benefit of being global in scope, making it an efficient solution for controlling flow in applications where space is constrained. Although acoustic flow control has been demonstrated to be effective in low-speed applications [6,13], its applicability and efficacy in high-speed flows have yet to be conclusively demonstrated.

1.3 Motivation. In light of the lack of knowledge on acoustic flow control in high-speed applications, highly loaded turbine blades were tested in a linear cascade setup on various Mach conditions with and without excitation. Two different sound sources and orientations were considered. First, the flow was excited by a siren disk device (active) upstream of the blade row. Second, a Helmholtz resonator embedded in the tailboard (passive) of the linear cascade was utilized for downstream excitation. The results presented show the possibility of acoustic flow control in transonic flows. Further, the effectiveness of the active and passive flow control methods demonstrated here is of interest to the design community since they are suggestive of the feasibility of implementation in an engine. This is because the frequencies of excitation applied here via the siren disk are within the range typically associated with Tyler–Sofrin modes that arise due to blade-vane interaction in operating engines [26]. Also, the implementation of a Helmholtz resonator in an operating engine is well within the realm of possibility, considering current turbine manufacturing methods.

2 Methodology

2.1 Reduced-Order Geometric Model. A series of low-pressure turbine (LPT) airfoils [27] were designed to explore the limits of the expanded design space that was made possible by the development and application of reduced-order models for boundary layer transition [28,29]. It was shown that airfoils with design values of the incompressible Zweifel coefficient as high as 1.78 could operate over a wide range of conditions without encountering substantial flow separations that cause a dramatic rise in airfoil losses [30]. Accordingly, it was decided to design new airfoils for investigation here featuring even larger levels of lift (Zweifel = 2.10) that might benefit from the application of flow control at off-design conditions consistent with high altitude operation. Figure 1 charts predicted loss versus Reynolds number for three candidate airfoils, including the previous design at Zweifel = 1.78. The predicted behavior of the airfoils was investigated by running Reynolds-averaged Navier–Stokes simulations with transition modeling using ADS Code Leo [31], as previously discussed in Ref. [27]. The inlet total and exit static pressures were defined as boundary conditions. The simulations were used as a complementary tool for the interpretation of the experimental findings discussed in subsequent sections.

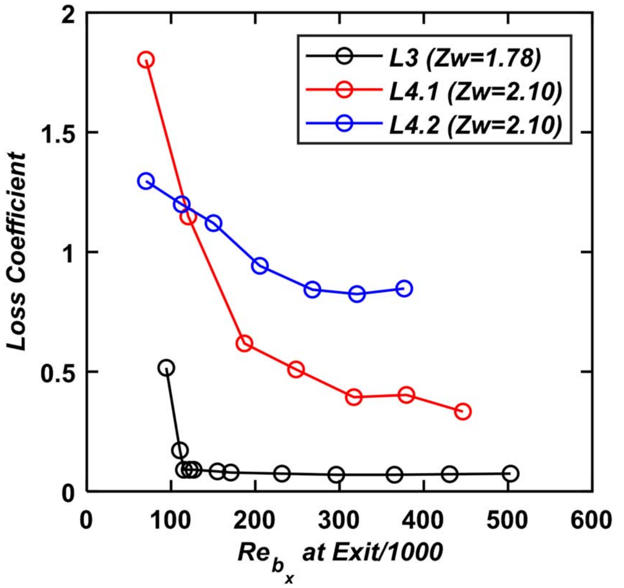

Fig. 1 Predicted loss versus Reynolds number variations for airfoils of interest

Note that here the variation in Reynolds number was achieved by altering the boundary conditions for inlet total pressure and exit Mach number for the airfoils at a constant exit static pressure equal to atmospheric conditions. For the airfoil with a design Zweifel = 1.78 (L3FHW), there is very little appreciable increase in loss for a very wide range of Reynolds numbers down to the lowest value plotted (consistent with an exit Mach number of 0.2). Accordingly, additional airfoils were designed to push the Zweifel coefficient beyond two to ensure that the application of flow control was warranted to improve blade performance. So, the remaining airfoils (L4FHW, L4.1, and L4.2) experience some level of separation even at high Reynolds numbers.

The increase in predicted loss for the L3FHW airfoil at Reynolds numbers below 100k is attributed to unreattaching separation, and this is in keeping with well-established effects of boundary layer separation on turbine efficiency [6,17]. Such separations increase the loss through the airfoil passage while at the same time reducing the overall lift on the blades, while inhibiting flow turning through the row. The predicted loss versus Reynolds number behavior of the L4FHW airfoils is indicative of substantial separation even at high Reynolds number conditions. The intent of the flow control application in this study is to reduce the severity of separations on the L4FHW airfoils, and it is believed that a demonstration of improved airfoil loading due to acoustic forcing would also result in a reduction in loss across the blade row and improvement in flow turning, in keeping with observations in Refs. [6,17].

2.2 Transonic Linear Cascade Setup. The Technion transonic linear cascade was utilized to perform the flow control study on the turbine blades. Driven by a screw compressor operating at a pressure ratio of 7:1, the cascade setup can operate in both open-loop and closed-loop modes; however, this study focused solely on results with exhaust pressure at atmospheric conditions. The cascade is designed to adjust incidence and stagger angles within a ±20-deg range without requiring major modifications to the test section. It also accommodates blade down-scaling if needed. The quick swap design allows for easy replacement of vane geometry and permits the use of a wide variety of airfoil geometries. At the exhaust, the cascade outlet is engineered to handle a broad spectrum of flow turning angles, ensuring it meets various testing requirements [32].

Figure 2 illustrates the main test section subassemblies along with the reference frame. The subsections include an inlet (1), a flow straightener and turbulence grid (2), controllable main frame frontboards (3), a bladed test section (4), an optical access window (5), rotating disks (6), controllable main frame perforated tailboards (7), and an outlet (8). To conduct the flow control study, L3FHW and L4FHW high-speed turbine blades are considered due to their loading characteristics and the separation behavior. The blades were scaled in size to fit into the linear cascade, retaining solidity. Five blades were placed into the cascade by the inserts mounted on the optical access windows, ensuring the flow periodicity [33]. The turbulent intensity was determined to be 4.7% based on Schlieren image analysis, aligned with previous work in the test facility [32]. The observation window is made from sapphire, which has more than 90% transparency for a transmission range of 0.15–5.5 μm.

The compressor set total pressure and the total pressure at the leading edge of the passage have a discrepancy due to the pressure losses on the pressure transmission line. Therefore, a calibration run is needed after changing each set of blades. Then, the isentropic Mach number was calculated by the inlet total and the exit static pressures. The total pressure was measured at the inlet of the blades using a Vectoflow Kiel probe. Static pressure measurements were performed at the downstream of the vanes through the pressure taps on the cascade walls [32]. To reach desired flow conditions, a correlation between isentropic Mach number (M_{isen}) and the compressor set pressure (P_{t_2}) was generated through the isentropic relation.

2.3 Acoustic Sources for Flow Excitation

2.3.1 Siren Disk. As one of the acoustic excitation mechanisms, an in-house siren disk mechanism was used. The working principle of the siren disk is the alternating interruption of an air jet by a rotating disk that has circumferentially placed holes on its body. It was designed to generate sound frequencies between 1 and 53 kHz, while reaching rotational speeds up to 40 kRPM. The system has the potential to reach 140 dB and is also correlated with the upstream pressure of its inlet. Figure 3 portrays the layout of the siren disk design.

The main components of the siren disk are draining valve (1), cable pass (2), inlet tube fitting (3), high-pressure tube (4), brushless DC (BLDC) electric motor (5), modular upstream nozzle (6), modular downstream nozzle (7), outlet cut-off valve (8), adjustable nozzle housing (9), disk (10), shaft (11), and high-speed coupling (12). The siren disk is driven by a BLDC motor controlled by a controller card. A high-pressure N_2 cylinder (200 bars) is used to supply sufficient and continuous upstream pressure to the device. The generated aero-acoustic sound is transferred to the cascade by a flexible hose, fixed to the spanwise opening located upstream of the test section (see Fig. 2).

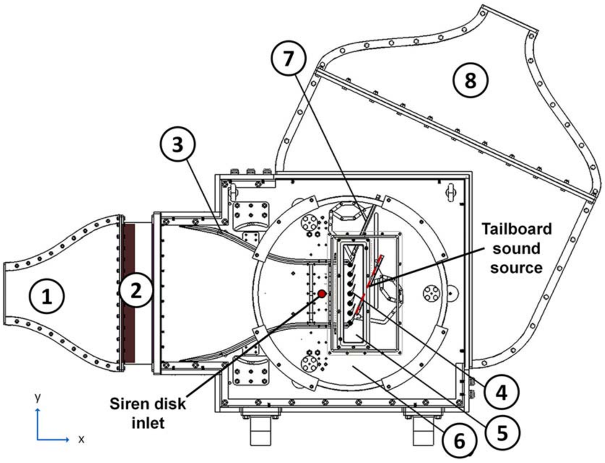

Fig. 2 Technion transonic linear cascade layout [32]

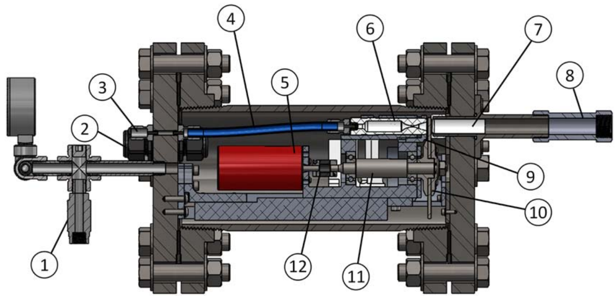

Fig. 3 Siren disk layout

The hole configuration on the disk plays a crucial role in obtaining the highest sound pressure level. A set of microphone measurements were taken at the siren outlet by changing the shape and the number of holes. Yielding the highest dB value in the widest spectrum, the geometry with 80 slots that has a 2.5-mm width was chosen as it has the capability to reach up to 140-dB sound pressure level (SPL).

2.3.2 Perforated Tailboard as Helmholtz Resonator. The alternative source of acoustic excitation is the use of a Helmholtz resonator. Such a device must include only a cavity and a small opening. It works on the principle of resonance, where the air inside the cavity is self-excited and vibrates at a natural frequency determined by the size and the shape of the cavity and the opening, resulting in tonal noise with a high sound pressure level potential. In the current case, the perforated tailboard was used as a Helmholtz resonator (see Fig. 4). The tailboards have an essential role in reaching temporal stability and spatial periodicity [32]. Thirty-seven perforations with a 3-mm diameter were placed on the surface of the tailboards, which open to the cavity behind the front panel of the tailboard. The cavity dimensions are 4 mm × 173 mm × 29.7 mm, which leads to the resonance frequency of 3.56 kHz by theoretical calculations. An estimated 3.6-kHz resonance frequency is observed as a significant spectral peak at the fourth harmonic, 14.25 kHz, for the design Mach number, 0.78.

The tailboard on the suction side of the blade array (Fig. 2) is exposed to a region of extremely high pressure near one end of the plate. As the flow turns, it drives the perforations on the tailboard with the empty volume behind the board acting as the resonator's blower. Unlike the siren disk, the Helmholtz resonator generates sound with improved tonality, and the sound waves are introduced from the downstream side of the cascade. The frequency range generated by one tailboard geometry is limited; however, the cascade flow naturally exhibits a broadband range of Kelvin–Helmholtz frequencies in the separating shear layer, encompassing at least one harmonic of the noise produced by the tailboard. A slight adjustment of the tailboard angle (∼10 deg) allows for control of the excitation frequency within 5% of the audible range. Nonetheless, the design angle was maintained to ensure a

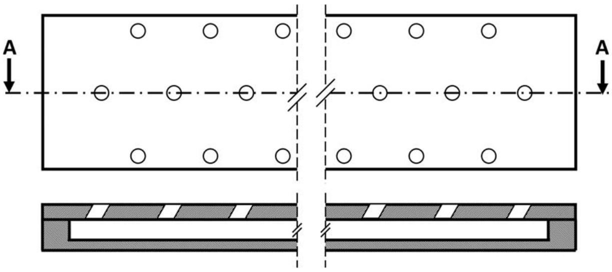

Fig. 4 Design of the tailboard front plane [32]

proper comparison with the unexcited data. Followingly, a series of microphone measurements taken from the downstream of the cascade, the tailboard performed an average 106-dB SPL through several Mach numbers, providing highly tonal sound at high SPL levels—at least 20 dB above the flow's natural broadband noise.

2.4 Measurement Techniques and Uncertainty Quantification

2.4.1 Static Pressure Measurements. The cascade is equipped with total and static pressure measurement capabilities that allow for evaluating correct operating conditions and aerodynamic performance of the turbine blades. For all pressure measurements on the test setup, 16-channel Scanivalve DSA3217 differential pressure transducers were used, with two different ranges (0–103 and 0–689 kPa) (full-scale accuracy of $\pm$0.05%). Static pressure was measured at a 5-Hz sampling frequency for 60 s, averaging 300 samples for each measurement.

Test section upstream and downstream static pressures are obtained by pressure taps providing minimal flow interference [32]. The hole length and the diameter were chosen as 0.5 mm with a measurement error of $\sim$0.3% [34]. The inlet and the exit traverse total and static pressure measurements are performed by a Vectoflow Kiel probe, which has a 0.9-mm head diameter (blockage of 3.6%). The angle error lies between $\pm$0.5 deg for flow angles within 60 deg. The probe is connected to the YZ traverse mechanism. The inlet uniformity measurements were taken at three M_{isen} conditions from 45 points, including 3 spanwise and 15 pitchwise locations. The incoming flow presented spatial uniformity of 99.7% and 99.3% for total and static pressures, respectively.

Additionally, static pressures are measured along the blade surfaces, providing information about aerodynamic loading. Figure 5 shows a representative image of the blades with internal static pressure measurement channels and illustrates their manufacturing process. The 2D scaled airfoil coordinates are extruded to obtain 3D blade geometries. Before printing the static pressure channels, an extra layer of sacrificial material was added to enable further machining. The printing process was performed on an EOS M290 printer using 17-4 *p*H stainless steel. The hole diameters are selected as close as the design guidelines (0.6 mm) due to the manufacturing constraints. The arithmetic average surface roughness (R_a) of the printed blade was measured using the Mahr MarSurf PS 10 and determined to be 12.2 μm. The blade production is completed after the finishing process by a computer numerical control (CNC) operation (surface roughness of the finished product, $R_a =$ 0.2 μm). Then, the surface static pressures are measured from 7 points on the surface of the airfoils.

2.4.2 Schlieren Imaging. A z-type Schlieren configuration [35] was selected, considering the space limitations on the optical tables, and the feasibility for the large region of interest in the test section. Figure 6(*a*) depicts the optical layout of the current Schlieren setup utilized in this study.

The setup consists of a light source (LED) (1), an aspherical condenser diffuser lens (2), iris-A (3), a condenser lens (4), iris-B (5), plane mirrors (6), parabolic mirrors (7), a razor blade edge (8), a high-speed camera (9), optical tables (10), cascade (11), blade test section (12), and a computer (13). The monochrome LED light source was used, which emits light at a wavelength of 528 nm and deliver a luminous flux of 3640 lumens. To control the scattering of the light and distribute uniformly, $f = 40$ mm Thorlabs aspherical condenser diffuser (600 grit) lens was placed in front of the light source. The definition of the light beam is controlled by a large iris (iris-A, 36 mm maximum aperture) after the primary lens. The light then passes through another condenser lens ($d = 50$ mm, *f*/1). The converged light beam goes through to the second iris (iris-B, 12 mm maximum aperture), generating a circular, fully uniform point light source before being reflected by a

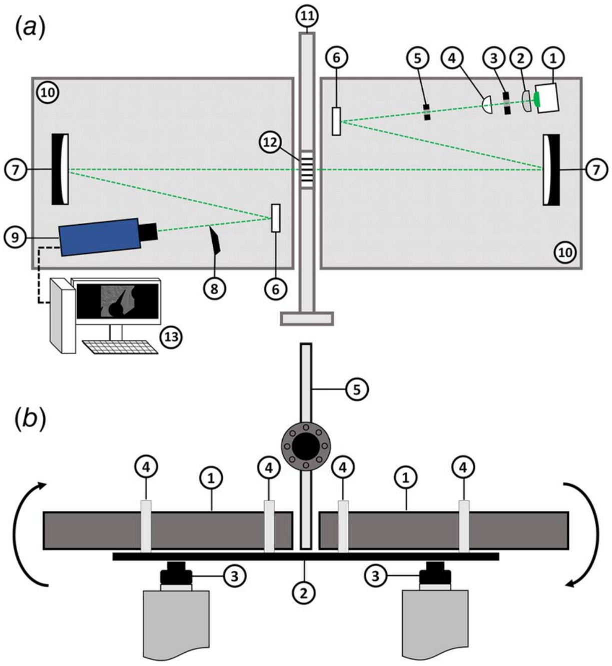

Fig. 6 (*a*) Components and optical layout of double-folded Schlieren setup for Technion transonic linear cascade (top view) and (*b*) optical table assembly (side view): (1) Nexus optical table, (2) aluminum breadboard, (3) dampener air cushions, (4) custom made mounting clamps, and (5) linear cascade

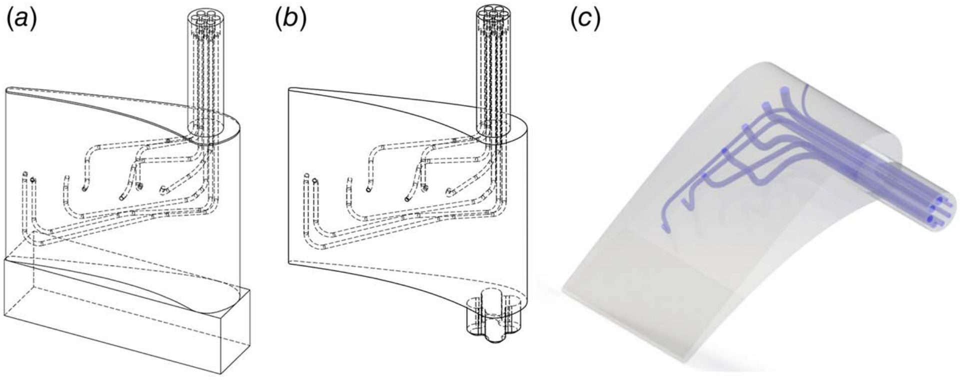

Fig. 5 (*a*) 3D printed turbine blade with internal channels, (*b*) blade after machining process, and (*c*) sample 3D view of a finished blade

plane mirror. Besides creating a well-defined, effective light beam, the slit-source iris enables adjusting the amount of light that passes through the Schlieren object. All elements until this point are aligned over the same optical axis by the Thorlabs precision post. To prevent the light from leaking to the other side of the cascade and reaching the camera lens, the aligned optical arrangement was enclosed in a 3D printed cover. The incoming light is reflected by an Edmund Optics plane mirror (100 mm × 100 mm, $\lambda/4$ protected silver coating), reaching the first Edmund Optics parabolic mirror ($d = 203.2$ mm, *f*/5, 40 in. FL Enhanced Aluminum) that collimates the beam perpendicular to the test section. Further, the diameter of the beam is equal to the mirror diameter since the iris-B is placed at the focus of the parabolic mirror. The light beam proceeds across the test section with the optical allowance of sapphire windows. To maintain symmetry along the optical axis and reduce coma and astigmatism aberrations, the parabolic mirrors must be positioned identically on both sides, as noted in Ref. [35]. The precise placement of the components is determined by minimizing the offset angle and taking the focal lengths into account. The symmetrical arrangement of parabolic and plane mirrors is made on the opposite side of the linear cascade, creating a focal point between the second plane mirror and the camera. The most critical task in the optical setup is partially obstructing the light to form the density gradients while obtaining a uniform background when there is no flow. This is achieved by positioning a razor blade in the light path before the camera captures the image.

When there is no cut-off with sufficient light intensity, the image entirely saturates. The placement of the blade plays an essential role in obtaining a uniform background. The image gets darker from only one side in case if there is a slight shift of the blade edge from the focal point throughout the optical path. In the correct position, the background digital level becomes uniform across the entire flow field. In this setup, the razor blade edge is placed at a 54-deg angle, matching the angle of the current configuration of turbine blades' placement relative to the optical table. The gradients were adjusted to vary in the streamwise direction. A total of 372,721 images were recorded for each experiment by Photron Fastcam SA-Z at 192,000 fps with a resolution of 256 × 240 px. The high-speed camera was combined with a 150-mm lens to reach increased resolution for a smaller field of interest (single blade view). The entire Schlieren system was mounted on an optical table setup, including two optical tables (Thorlabs Nexus B6090B), an aluminum optical breadboard (Thorlabs MB60120/M), and four air dampeners (Thorlabs PWA075). The optical tables were connected using an aluminum breadboard, allowing for coordinated movement (see Fig. 6(*b*)). The air dampeners support the aluminum breadboard to float the Schlieren setup. The current configuration decouples the optical equipment from the vibrations generated by the cascade. Furthermore, it minimizes relative movement between the optical setups on both sides, ensuring a consistent cut-off during the experiments.

The calibrated Schlieren technique is employed in the present study [35,36]. Sensitivity of the calibrated Schlieren is defined as the smallest detectable change in density gradient. This is directly related to the dynamic range of the camera; in other words, a change in the digital level in two consecutive pixels. In general, the sensitivity could vary in the measurement region as the calibration curve is not strictly linear. However, light settings are kept such that the calibration curve is approximately linear in the range of interest of the density gradients in the flow. The sensitivity estimates in the present measurements are estimated to be about 0.001 kg/(m^3/mm) for a density-gradient range of 0.4 kg/(m^3/mm).

The vibration of the linear cascade at transonic speeds causes some fluctuations in the Schlieren measurements. The amplitude of density-gradient fluctuations for the horizontal cut-off of the knife's edge is found to be greater than that of the vertical cut-off. The uncertainties in the density gradient in the former and later cases, respectively, are 2% and 0.3%.

2.4.3 *Spectral Postprocessing Tools*

2.4.3.1 Short-time Fourier transform. The time-dependent Schlieren images of the flow fields vividly capture the unsteady flow characteristics. For instance, the shedding of coherent vortical structures within the separated shear layer occurs in distinct phases. At certain times, Kelvin–Helmholtz vortical structures are actively shed, while at other times, this shedding is absent. The underlying cause of the intermittent shedding of vortices remains uncertain and is perhaps linked to the low-frequency oscillations of the separated shear layer, often referred to as the "flapping" motion of the separated region [2,37–40]. Fourier transform of the full time-series renders an average picture of the spectra, and often fails to represent the transient flow dynamics accurately. Consequently, a short-time Fourier transform (STFT) is sought in the present investigation to address this limitation.

In the STFT, a "Hann" window length of 2048 (∼0.1 s of the time-series) with an overlap of 75% is applied. This configuration provides a spectral resolution of around 47 Hz, which is sufficient for the present study. The time-localized power spectral densities (PSD) obtained by the STFT are conditionally averaged to enhance the detection of the spectral peak [Each time-localized PSD is appropriately thresholded (3×10^{-7} kg/m^3/mm), where only the frequencies with power density exceeding the threshold are summed over to be averaged, while those below are disregarded. The conditionally averaged PSD is obtained by averaging 70 such thresholded STFTs. The resulting spectral peak is insensitive to variations in the threshold value, providing confidence in the robustness of the approach.]

2.4.3.2 Spectral proper orthogonal decomposition. For statistically steady flow fields, the space-time proper orthogonal decomposition can be extended to spectral proper orthogonal decomposition (SPOD) [41–43]. SPOD provides modes that oscillate at a single frequency and can be sorted according to their energy content. In the present study, the five most energetic modes at relevant frequencies are estimated. The energy of each mode is given by the square of the eigenvalue, which is associated with the cross-spectral density tensor $\boldsymbol{S}$ and weight function $\boldsymbol{W}$ (2-norm inner product in the spatial domain with uniform grid size) through the following eigenvalue relation:

$$\int \boldsymbol{S}(\boldsymbol{x}, \boldsymbol{x}', f) \cdot \boldsymbol{W} \cdot \phi(x, f) = \lambda(f)\phi(\boldsymbol{x}', f) \qquad (1)$$

$\phi(\boldsymbol{x}, f)$ is the eigenfunction (or the mode-shape) corresponding to the frequency f. λ is the corresponding eigenvalue that is a function of f; λ^2 represents the energy content of the eigenmode $\phi(\boldsymbol{x}, f)$ (where $\phi(\boldsymbol{x}, f)$ itself is a normalized quantity). In the present SPOD analysis, the numerical method of Ref. [44] is employed, and 10^5 total sequential fields with a 192-kHz uniform sampling rate are utilized. The frequencies of interest in the flow are higher than 250 Hz, resulting in a block size of 1024 sequential fields. The cross-spectral density tensor $\boldsymbol{S}$ is estimated using the Welch's method with a "Hamming" window function and 50% overlap between two blocks. The mode shapes and their energy are obtained by averaging about 200 blocks. It is found to be robust to changes in block size and the overlap percentage.

2.4.3.3 Blob analysis. Acoustic excitation affects the size of vortical structures within the separated shear layer. The intense white and dark regions are particularly significant as they indicate the presence of these vortical structures. To capture the vortices, Schlieren images are binarized using an appropriate threshold (1.5×10^{-3} kg/m^3/mm). The binarized image is then processed using the MATLAB function "regionprops," which calculates the size of connected bright regions. This provides a close approximation of the actual size of the vortical structures. Such structures predominantly appear in the suction surface of the blade, particularly within the separated shear layer. A statistical distribution of the vortex sizes is then generated, illustrating their relative change in excited flow compared to unexcited flow.

3 Results

3.1 Baseline Flow Fields. Open- or unreattaching separation is observed for L4FHW-HS, and not for L3FHW-HS. The unexcited Schlieren fields and static pressure measurements along the suction surface of the blades are presented in the following. In the current investigation, the Mach and Reynolds numbers are not independent of each other. The Mach–Reynolds dependence plot is shown below.

3.1.1 Blade Static Pressures. Among the five blades mounted inside the linear cascade, only the center airfoil and its neighboring blades included pressure tappings with internal channels. Thus, the time-averaged periodicity was confirmed by surface static pressure distributions on two consecutive blades and downstream total pressure traverse measurements, with wake profiles showing a correlation of $R = 0.96$. Then, pressure measurements were normalized as $C_p = (P_{t_i} - P)/(P_{t_i} - P_{s_e})$, where P is the static pressure on the blade surface, P_{t_i} is the inlet total pressure and P_{s_e} is the exit static pressure. The uncertainty of the pressure coefficient (C_p) was calculated to be ±0.058.

For the L3FHW and L4FHW airfoils at $M_{\text{isen}} = 0.5$ ($\text{Re}_{B_z} \sim 150,000$) and 0.78 ($\text{Re}_{B_z} \sim 250,000$), the C_p distributions acquired from experiments and computational fluid dynamics (CFD) are shown in Fig. 7. All the experimental data indicate clear peak suction regions except Fig. 7(*a*). Due to subsonic conditions and the highly loaded design nature of L4FHW blades, the flow separates before reaching the peak pressure; therefore, it cannot accelerate further, observed with a plateau region through full chord. As the Mach number increases to 0.78 in Fig. 7(*b*), the peak region becomes more significant. Subsequently, the flow gradually accelerates toward the mid-chord, followed by a separation region around $0.3 < x/B_x < 0.6$ (laminar separation bubble formation). Eventually, the flow reattaches with a sharp gradient. Finally, in the experimental analysis of the L3FHW blades (Fig. 7(*c*)), the initial deceleration of the flow is distinctly observable, as it occurs immediately downstream of the first pressure tapping location. The flow then accelerates, reaching a region characterized by a less pronounced pressure gradient within the range ($0.4 < x/B_x < 0.55$). This may mean a small separation bubble forming and decaying immediately, with no significant separation.

This is unsurprising given that the lift level of the L4 airfoils exceeds twice the historically accepted ideal level. Hence, notable discrepancies are seen in Figs. 7(*a*) and 7(*b*). CFD shows a fully attached flow characteristic, while the experimental results highlight an early and massive separation, especially in lower Mach conditions.

On the other hand, in the relatively lower loading L3FHW blade, there is good agreement between the CFD and experimental results. Again, this means that the expanded LPT design space enabled by the modeling techniques encompasses lift levels approaching 1.8.

3.1.2 Schlieren Images. For the L4FHW case with significant separation, the time-averaged Schlieren fields are charted in Fig. 8 presenting the line-of-sight density gradients for the two isentropic Mach numbers.

The arrows show the direction of the flow inlet and outlet, whereas the direction of the gradients with respect to the blade's edge is given on the bottom right corner of each image. The darker areas in the vicinity of the suction surface (highlighted with dashed circles) of the blade are an indication of the separation region. Although the blade inserts (circular black area) create blind spots on the image, separation can be inferred to occur near the leading edge of the blade based on readily developed shear layer and pressure measurement results.

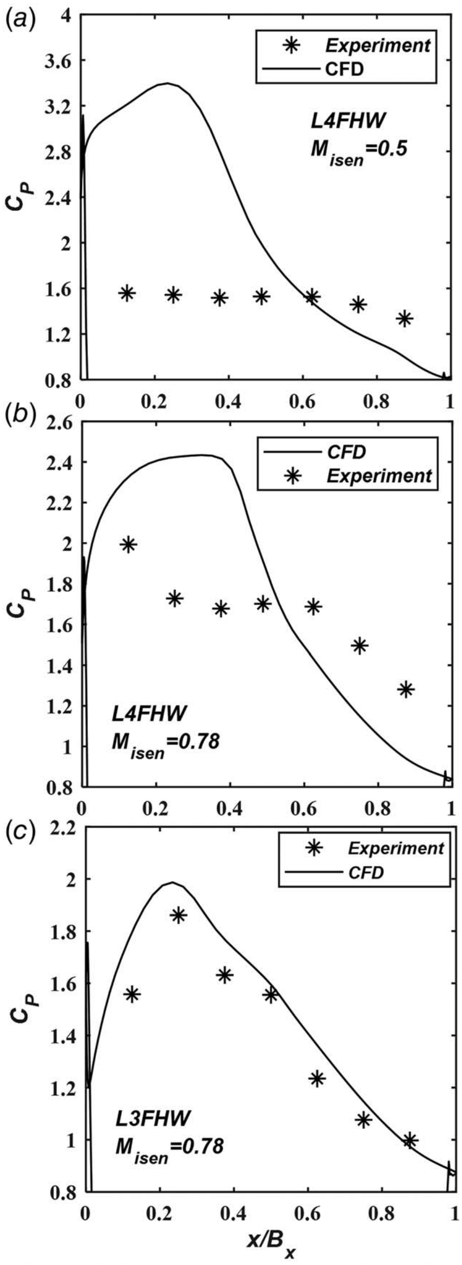

Fig. 7 Midspan C_p distribution comparisons of CFD and experiments on L4FHW at (*a*) $M_{\text{isen}} = 0.5$ and (*b*) $M_{\text{isen}} = 0.78$ and (c) on L3FHW at $M_{\text{isen}} = 0.78$

3.1.3 Evaluation of Kelvin–Helmholtz Frequency. The separated shear layer is inviscidly unstable, well-known as the KH instability. The most amplified KH instability frequency scales as $f_{\text{KH}} \propto U_\infty^{3/2}$ [4,13]. This scaling has been primarily observed in separated shear layers at low speeds. At relatively high Mach number flows, when compressibility becomes important, the most amplified frequency scaling is modified.

Figure 9 shows the PSD at a point marked by the white cross in the Schlieren image in Fig. 9(*b*), positioned in the separated shear layer with different isentropic Mach numbers. The peaks represent the most amplified KH modes, which scale as $f \sim M_{\text{isen}}^{3/2}$. The abscissa is then rescaled as $f/M_{\text{isen}}^{3/2}$ revealing this scaling as a vertical line (black dashed line) at $f/M_{\text{isen}}^{3/2} \approx 24,000$.

However, as Mach and Reynolds numbers are not independent in the current study, this scaling can also be considered to represent Reynolds number (as commonly done in low-speed literature

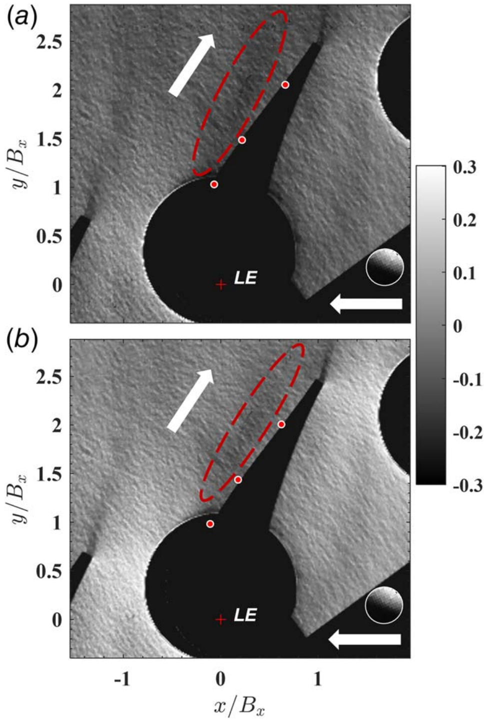

Fig. 8 Baseline mean Schlieren fields: (*a*) $M_{\text{isen}} = 0.5$ and (*b*) $M_{\text{isen}} = 0.78$ for L4FHW blades

[4,13]). Table 1 summarizes the most amplified KH frequencies and the corresponding Strouhal number (St) for their exit isentropic Mach number.

In the following sections, the static pressure along the blade's suction surface, the spectral content, and the blob analysis are presented for the siren-excited flow field.

3.2 Excited Flow Measurements With Siren Disk. At a constant rotational speed, the siren disk is operated at different upstream plenum pressure ratios to modulate the SPL of the acoustic excitation. Table 2 summarizes the operating conditions of the siren disk. The excitation frequencies at the two different isentropic Mach numbers are selected based on the spectra of the unexcited Schlieren field in Fig. 9. It is important to note that, due to the physical mechanism of sound generation by the siren disk, the sound's tonality is not achieved at satisfactory levels. The generated sound often contains harmonics and subharmonics of the fundamental frequency.

3.2.1 Blade Static Pressures. Figure 10 compares the C_P of the excited and unexcited flows at the two isentropic Mach numbers for L4FHW blades. As already discussed, the unexcited flow is identified with a massive separation, especially at $M_{\text{isen}} = 0.5$ since there is only a slight recovery supported with a moderate favorable gradient. Along with that, at $M_{\text{isen}} = 0.78$, a laminar separation bubble formation is noted.

A significant effect is observed at $M_{\text{isen}} = 0.5$ with the excitation at 127, 130, and 139 dB. Sixty percent peak suction rise is achieved, and flow is further accelerated in the proximity of the trailing edge, providing a better recovery. Notably, 127 dB is identified as saturation SPL, beyond which no further changes in the pressure distribution are detected.

Similarly, the influence of acoustic excitation is present for $M_{\text{isen}} = 0.78$ (see Fig. 10(*b*)). The peak suction pressure increases steadily with the SPL of the imposed sound. However, the nonlinear gain observed at 140 dB is particularly intriguing. The peak suction pressure shifts downstream, accompanied by an increase in its magnitude (15%). Overall, both cases portray promising improvement in the value of achievable peak suction and pressure recovery.

It is important to mention that an unsteady jet exiting the siren disk is injected $7B_x$ far upstream from the blades. The jet's mass flow rate is approximately 1.2–2% of the oncoming mass flow rate per passage, which is small and unlikely to significantly alter the C_p distribution over the blades. Therefore, we attribute the observed rise in peak suction to acoustic excitation.

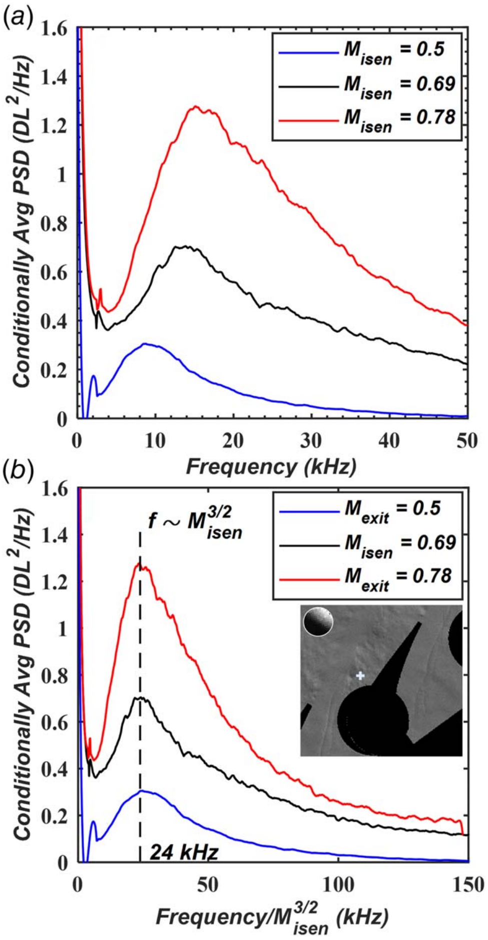

Fig. 9 (*a*) Conditionally averaged spectra of L4FHW blades under three Mach conditions and (*b*) scaling of the most amplified frequency with isentropic exit Mach number. The time-series was probed at $[x/B_x,\ y/B_x] = [-0.072, 0.53]$.

Table 1 The most amplified frequencies for L4FHW blades at different isentropic Mach numbers

M_{isen}, Re_{B_x}	Most amplified KH frequency (kHz), St
0.50, 150,000	8.8, 1.32
0.69, 215,000	12.1, 1.42
0.78, 250,000	15.56, 1.5

Table 2 The operating conditions of the siren-disk at two different isentropic Mach numbers

M_{isen}	Excitation frequency (kHz), St	SPLs (dB)
0.5	8.8, 1.32	127, 130, 139
0.78	15.56, 1.5	128, 133, 140

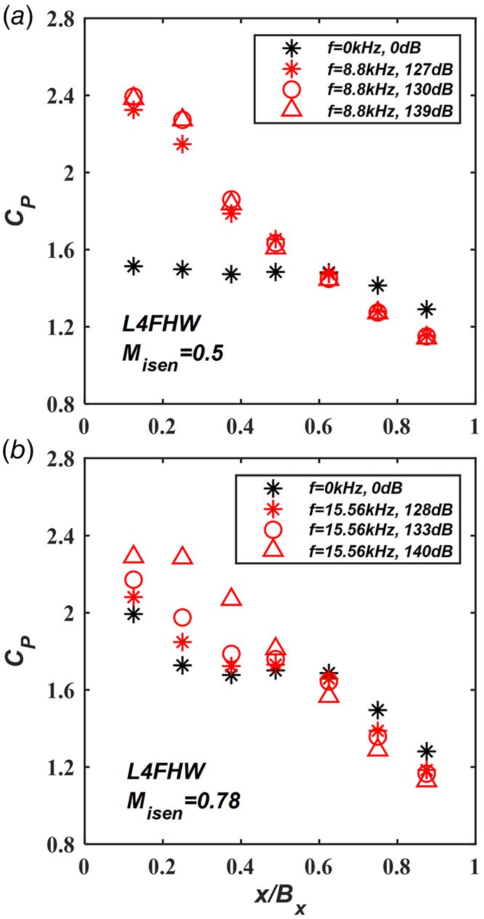

Fig. 10 Midspan C_p distribution comparison of the unexcited and siren disk excited flows at (*a*) $M_{\mathrm{isen}} = 0.5$ ($f = 8.8$ kHz) and (*b*) $M_{\mathrm{isen}} = 0.78$ ($f = 15.56$ kHz)

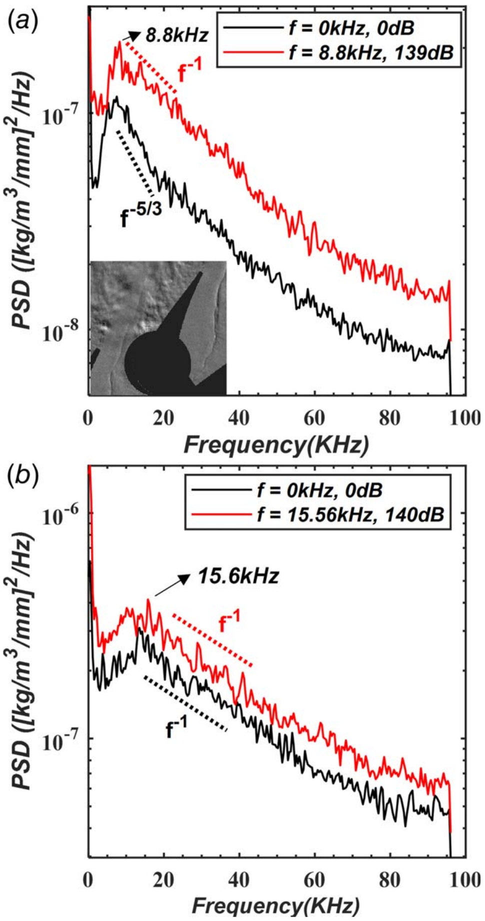

Fig. 11 Full time-series PSD comparison of the unexcited and siren disk excited flows for (*a*) $M_{\mathrm{isen}} = 0.5$ ($f = 8.8$ kHz) and (*b*) $M_{\mathrm{isen}} = 0.78$ ($f = 15.56$ kHz). The spectra acquisition location is also indicated in (*a*). The scale variations are shown with dashed lines.

3.2.2 Fast Fourier Transform Spectra. The spectral signatures at $M_{\mathrm{isen}} = 0.5$ and $M_{\mathrm{isen}} = 0.78$ are presented in Fig. 11. The flow is energized considerably when acoustic excitation is introduced, as indicated by the area under the red and black curves at both Mach numbers. An upward PSD shift during excitation may indicate an intensification of density-gradient fluctuations, potentially associated with increased mixing. The extent of this energization is lower for $M_{\mathrm{isen}} = 0.78$ compared to $M_{\mathrm{isen}} = 0.5$. This is reflected in the change in the angle of the separated shear layer, which is more pronounced at the lower Mach number.

In a fully developed turbulent flow, the spectrum in the inertial subrange varies as $f^{-5/3}$, whereas the low-frequency (large-scale) and the high-frequency (small-scale) regions of the spectrum vary as f^n with $n > -5/3$ and $n < -5/3$, respectively. The behavior of the spectra is expected to be similar to a velocity time-series spectrum. The spectrum of the unexcited flow at $M_{\mathrm{isen}} = 0.5$ in Fig. 11(*a*) around the KH frequency goes as $f^{-5/3}$, which signifies the intermediate scale including mixed structures in terms of frequency and length scale. However, upon acoustic excitation, the spectrum goes as f^{-1} indicating dominance of large-scale coherent density gradients often seen in jets and wakes. This could be indicative of the fact that energy is injected into these frequencies, and the large-scale, organized KH dynamics are dominant upon excitation. At $M_{\mathrm{isen}} = 0.78$, the frequency variations for both unexcited and excited flows exhibit a proportional relationship to f^{-1}. Likely due to the dominance of large-scale structures in the unexcited flow attributed to the compressibility effect, no significant change is induced with the sound introduction. The presence of local weak shock structures within the flow further supports this observation.

3.2.3 Variance of Intensities. Figure 12 presents the variance of the Schlieren fields. Since it is challenging to visualize separation directly from Schlieren images, the peak variance distribution of the Schlieren time-series serves as a reliable indicator of the time-averaged separated shear layer. To evaluate the shear layer angle, 12 lines perpendicular to the suction surface are placed along various streamwise locations. The shear layer position is then determined by analyzing the density-gradient variance profiles along these lines, where local maxima indicate its local position. Finally, an overdetermined least-squares linear fit of these successive maxima points is considered to represent the shear layer and its angle. Figures 12(*a*) and 12(*b*) are the variance fields for unexcited and excited flow at $M_{\mathrm{isen}} = 0.5$, while Figs. 12(*c*) and 12(*d*) present the corresponding variance fields at $M_{\mathrm{isen}} = 0.78$. The peak variance region near the blade, labeled shear layer ("SL") in all figures, with dashed lines indicating the time-average shear layers. A change in the angle of the separated shear layer was observed when the flow is excited, measuring 10 deg for the $M_{\mathrm{isen}} = 0.5$ and 8 deg for the $M_{\mathrm{isen}} = 0.78$. This shift of the separated shear layer angle is a measure of the amount of flow control that is achieved. Furthermore, the spread of the shear layer is suppressed as shown in Figs. 12(*b*) and 12(*d*) with the assumable reduction of drag losses.

3.2.4 Blob Analysis. A vortical structure creates a localized low-pressure region, visible as bright and dark patches in Schlieren images. A threshold of 1.5×10^{-3} kg/m^3/mm is applied on the fluctuating fields before binarization. The resulting white and black

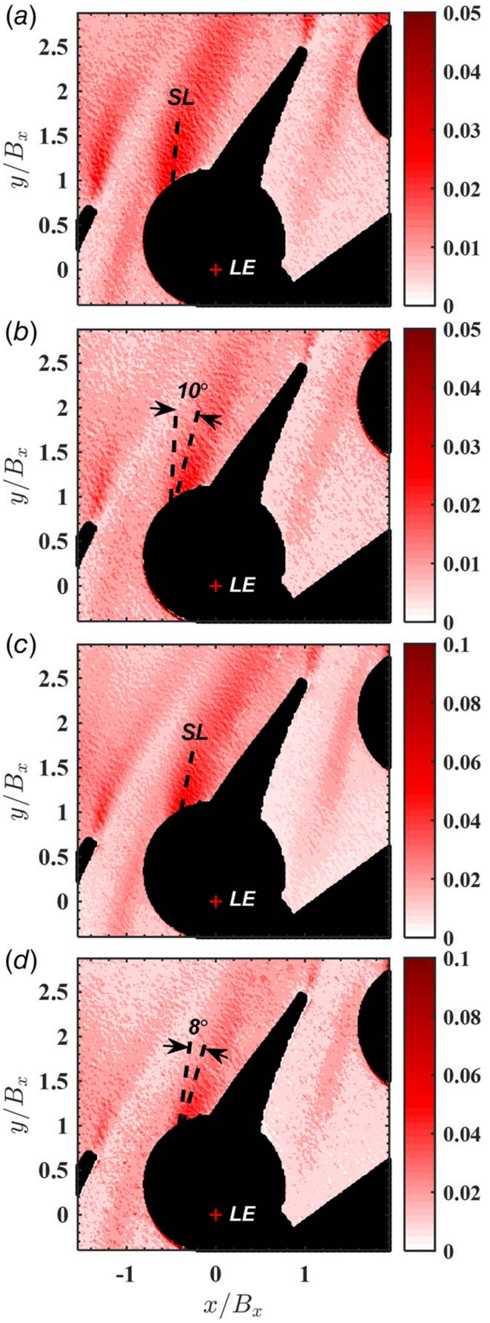

Fig. 12 Variances of the fluctuating Schlieren fields: (*a* and *b*) for the unexcited and siren disk excited cases at $M_{\text{isen}} = 0.5$ (f = 8.8 kHz), respectively, and (c and *d*) variances of the unexcited and siren disk excited (f = 15.56 kHz) cases at $M_{\text{isen}} = 0.78$. The change in SL angle is indicated with dashed lines.

regions in the shear layer of each Schlieren image are used to estimate the size of the vortical structures. Figure 13 compares the probability density function of the detected bright structures, representing vortices in the shear layer, for both unexcited and excited cases at $M_{\text{isen}} = 0.78$. The vortical structures in the excited flow appear relatively stronger than in the unexcited flow. Larger gradients indicate stronger mixing and associated flow control for separated flow recovery.

3.3 Excited Flow Measurements With Perforated Tailboard. The perforated tailboard (a Helmholtz resonator), capable of producing 3.56-kHz sound production (assuming all 37 perforations are operational based on the oncoming flow orientation), was used as an alternative method to excite the flow. The following sections present the results for suction side pressure distribution, spectral analysis, SPOD modes, and blob analysis.

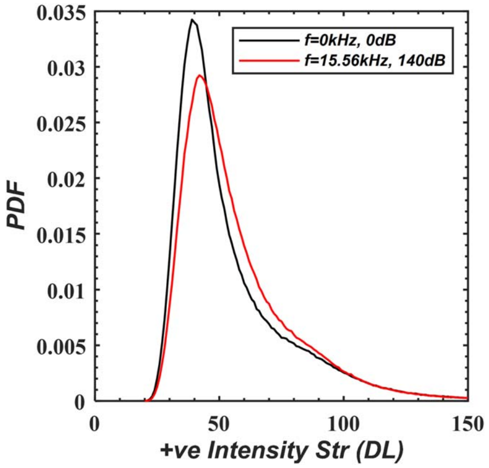

Fig. 13 Probability density function of bright structures representative of vortices at $M_{\text{isen}} = 0.78$

3.3.1 Blade Static Pressures. The flow was excited by two main frequencies: 13.9 kHz for $M_{\text{isen}} = 0.69$ and 14.3 kHz (the fourth harmonic of the tailboard's calculated natural frequency) for $M_{\text{isen}} = 0.78$. The difference in excitation frequencies is due to a change in Rossiter frequency, based on Mach number. The SPL value is measured much lower than the siren disk, standing at around 106 dB. For the unexcited measurements, the tailboard was covered with an aluminum tape to prevent the resonation mechanism. Figure 14 shows the pressure distributions over the L4FHW blades for $M_{\text{isen}} = 0.69$.

For the $M_{\text{isen}} = 0.69$ case, the pressure distribution remains the same (within the error margin) until $x/B_x = 0.5$ for both unexcited and excited cases. Clear evidence of a separation bubble is observed between $x/B_x = 0.36$ and 0.62. Beyond this region, with acoustic excitation, a steeper pressure gradient is observed compared to the unexcited case, suggesting that the separation bubble dissipates more rapidly under actuation. It appears that the sound pressure level is insufficient to alter the pressure distribution near the leading edge, as no change in peak suction pressure is detected. However, the modifications near the trailing edge demonstrate the

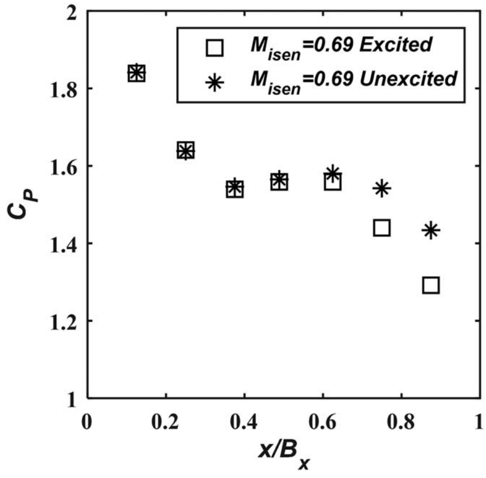

Fig. 14 Midspan C_p distribution comparison of the unexcited and tailboard excited flows at $M_{\text{isen}} = 0.69$ (f = 13.9 kHz)

impact of the acoustic excitation. The $M_{\mathrm{isen}} = 0.78$ case produces similar results to those observed in the siren disk at the same Mach condition. However, the effects are less pronounced and are therefore not presented here.

3.3.2 Fast Fourier Transform Spectra. Figure 15 shows the fast Fourier transform (FFT) spectra at $M_{\mathrm{isen}} = 0.69$ for unexcited and excited conditions, probed near the suction surface at $x/B_x = -0.29$ and $y/B_x = 1.2$ away from the wall (shown with a white cross in Fig. 15(*a*)). Figure 15(*a*) displays the full time-series, while Fig. 15(*b*) presents the corresponding conditionally averaged short-time spectra.

A distinct, sharp peak at the resonator frequency is observed in the corresponding Mach number. Conditionally averaged PSD shows a more pronounced peak, along with an increase in energy content when excitation is applied. Unlike the full-time FFT, the STFT shows a reduction in fluctuation energy in the Schlieren fields when excitation is applied. This suggests that the shedding structures are more coherent as a result of the energy concentration on the excitation frequency. This is further demonstrated in the conditionally averaged STFT shown in Fig. 15(*b*), where the spectra (STFT) during the calm phases are essentially excluded from the averaging. Thus, acoustic excitation energizes the shear layer.

The spectra of the density-gradient time-series are given with Fig. 15(*a*) showing that for $M_{\mathrm{isen}} = 0.69$, in the frequency range around the KH instability frequency, the unexcited flow spectrum varies in the inertial subrange as $f^{-5/3}$, whereas the excited flow spectra in this range go as f^{-1}, demonstrating similar trends with the siren disk excitation. Again, this suggests that the structures became larger and more coherent with the acoustic actuation.

3.3.3 Variance of Intensities. The effect of acoustic excitation on the separated shear layer is quantified by the change in its angle, as was done for the siren disk excitation cases. Qualitative differences between the unexcited and excited variance of the Schlieren fields are evident in Figs. 16(*a*) and 16(*b*) for $M_{isen} = 0.69$. Acoustic excitation affects both the diffusion of turbulence in the separated shear layer and its angle. The change in the shear layer angle is found as 11 deg.

3.3.4 Spectral Proper Orthogonal Decomposition. The SPOD spectra and mode shapes for the unexcited and excited Schlieren fields are shown in Fig. 17. The unexcited spectra in Fig. 17(*a*) display a broadband KH frequency centered around 13 kHz. In the excited SPOD spectra, a significant peak is observed at the excitation frequency of 13.875 kHz that corroborates the microphone measurements.

The most energetic mode shapes at 13.875 kHz for the unexcited and excited Schlieren flow fields are shown in Figs. 17(*b*) and 17(*c*), respectively. The unexcited flow depicts the typical KH flow field (Fig. 17(*b*)), vortical structures having a wavelength of ∼$0.3B_x$. A significant distortion in the mode's wavelength is noticeable in the near-wake region with the excitation (Fig. 17(*c*)), likely due to the interaction between the acoustic wave and the blade wake. Additionally, a natural distortion of the wavelength is expected due to variations in the freestream velocity over the blade. References [10,45] highlighted the importance of wavelength reduction in the receptivity process during flow transition.

4 Discussion

Spectral analyses have clearly demonstrated the modifications of the flow structures under acoustic excitation, as well as small improvements in blade loading (as indicated by the C_p distributions). Short-time spectral analysis further highlights the transient

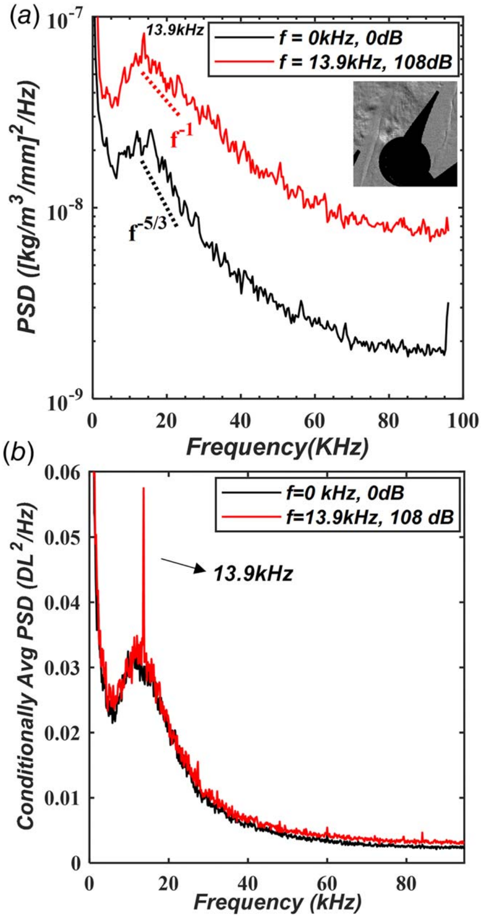

Fig. 15 (*a*) Full time-series FFT and (*b*) STFTs at $M_{\mathrm{isen}} = 0.69$ for unexcited and tailboard excited ($f = 13.9$ kHz) cases. The spectra acquisition location is also indicated in (*a*). The scale variations are shown with dashed lines.

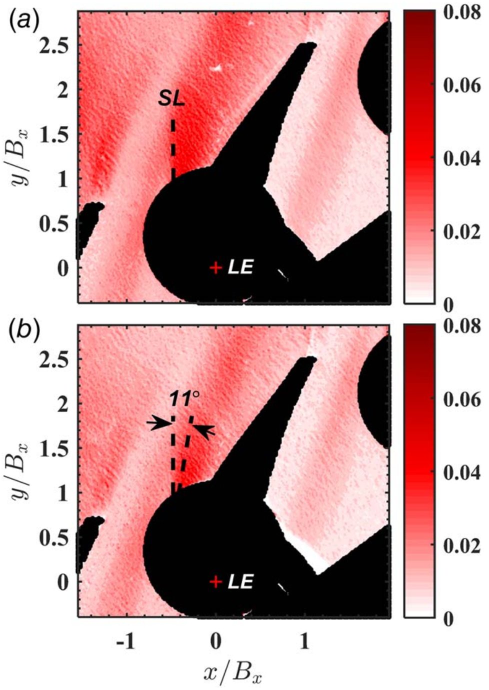

Fig. 16 Variances of the fluctuating Schlieren fields: (*a* and *b*) for the unexcited and tailboard excited cases at $M_{\mathrm{isen}} = 0.69$ ($f = 13.9$ kHz), respectively. The change in SL angle is indicated with dashed lines.

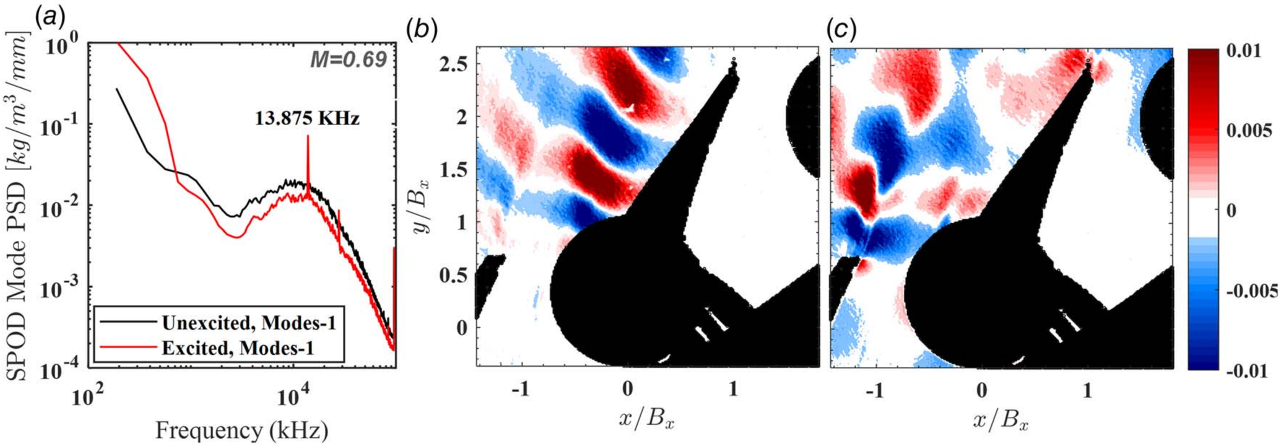

Fig. 17 (*a*) Unexcited and excited SPOD spectra of the most energetic modes at $M_{\mathrm{isen}} = 0.69$ for L4FHW and (*b* and *c*) the corresponding mode shapes for the unexcited and excited flows at 13.875 kHz, respectively

nature of the vortical structures, with phases where they are present and others where they vanish. This long-period phenomenon appears in the spectra as low-frequency activity, which may be linked to the flapping motion of the separated shear layer [37,38]. However, the underlying mechanism behind this low-frequency behavior is not yet well understood. It has been shown that this low-frequency activity is stronger in the presence of a laminar separation bubble compared to a fully open-wake separation [37,38,40].

Blob analysis revealed that the vortical structures are strengthened when the flow is acoustically excited, indicating increased coherence due to the acoustic waves. Similar behavior was observed in the low-speed experiments of Ref. [13], where acoustic excitation amplified the coherent accumulation of vorticity and its subsequent shedding at the excitation frequency. Unlike the low-speed C_p distributions, the current study shows only a modest rise in peak suction pressure. The reasoning behind this could be explained by three-dimensional, secondary flows occurring in the cascade flow.

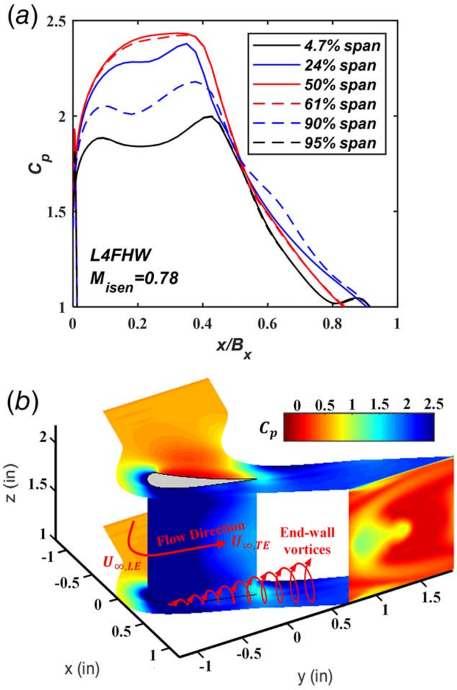

Fig. 18 (*a*) CFD pressure distributions of the L4FHW blade in various span locations and (*b*) C_p contours in the L4FHW turbine passage

To investigate the existence of secondary flows, a numerical simulation was conducted for the design $M_{\mathrm{isen}} = 0.78$ on L4FHW blades. The pressure distributions present that the three-dimensional secondary flow effects are indeed significant with nearly 40% peak suction pressure variation along the span of the blade, see Fig. 18(*a*). Figure 18(*b*) demonstrating the three-dimensional C_p distribution over a blade passage on the end walls and at the exit plane. The development of the end-wall boundary layer can be seen with the secondary flows of end-wall vortices. The structure is likely symmetrical across both the blade surface and the end wall, reflecting a mirrored configuration. Apart from the viscous effects, the development of the end-wall boundary layer can push the oncoming freestream toward the midspan region, increasing the freestream velocity from the leading edge to the trailing edge of the blade ($U_{\infty,\mathrm{TE}} > U_{\infty,\mathrm{LE}}$). This acceleration of the free stream is reflected in the pressure distribution on the blade. C_p can increase near the trailing edge as freestream pressure decreases due to strong secondary flows, compared to pressure distribution over the same blades with negligible secondary effects (i.e., blades with higher aspect ratio). The actuation of sound is believed to help control end-wall vortices and reduce the resultant effective blockage. This leads to a decrease in C_p mostly around the trailing edge, as observed in Fig. 14. We hypothesize that the lack of an increase in peak suction pressure, despite the changes in shear layer angles and the spectra, is due to 3D secondary flow effects.

5 Conclusion

An experimental investigation was conducted on high-lift, high-work blades (L3FHW, L4FHW) in a linear cascade setup to evaluate the potential of acoustic flow control under transonic conditions. Two acoustic forcing methods were employed: active upstream actuation using a siren disk, and passive downstream actuation via the cascade's perforated tailboard, functioning as a Helmholtz resonator. Siren disk achieved up to 60% increase in peak suction pressure and a 10-deg reduction in the separated shear layer angle. Similarly, tailboard excitation reduced the shear layer angle by 11 deg, demonstrating effective control. Blob analysis revealed enhanced size and coherence of vortical structures, supported by spectral evidence of inertial subrange scaling shifting from $f^{-5/3}$ to f^{-1}. While the tailboard offered modest pressure recovery near the trailing edge, numerical simulations identified significant secondary flow effects (end-wall vortices) as a limiting factor. Acoustic forcing primarily reorganized these vortices, indirectly influencing midspan pressure distributions.

Despite the challenges of implementing acoustic forcing in rotating turbine stages, the potential benefits are significant. This approach could enable a 15% reduction in engine weight, a 57%

decrease in LPT airfoil count, and an 8-cm reduction in engine length, with corresponding unmanned aerial vehicle (UAV) performance gains, including a 10% increase in range and endurance or a 0.8-km rise in operational altitude [13].

This study successfully demonstrated the feasibility of acoustic flow control in high-speed flows, providing valuable insights into its capabilities. These findings establish a strong foundation for future research and development, guiding the practical application of acoustic actuation in advanced turbine and engine designs.

Acknowledgment

We appreciate the assistance of Mr. Michail Tsinoglou with the Schlieren setup and processing of data. We thank Dr. Alexandros Terzis for his guidance. We also thank Professor Joe Lefkowitz and Dr. Si Shen for lending and helping us with the high-speed camera equipment.

Funding Data

- This research is supported by AFRL and *the* Minerva Foundation (AZ5746940764) and partly at the Technion by the Zeff Fellowship.

Conflict of Interest

There are no conflicts of interest.

Data Availability Statement

The datasets generated and supporting the findings of this article are obtainable from the corresponding author upon reasonable request.

Nomenclature

f = Focal length, frequency
x = Image frame x-coordinate
y = Image frame y-coordinate
P = Blade surface static pressure
$\mathbf{S}$ = Cross-spectral density tensor
$\mathbf{W}$ = Weight function
f_{KH} = Kelvin–Helmholtz frequency
B_x = Axial chord
C_p = Pressure coefficient
M_{isen} = Isentropic Mach number
P_{s_e} = Exit static pressure
P_{t_i} = Inlet total pressure
R_a = Arithmetic average surface roughness
U_∞ = Free stream velocity
Re_{B_x} = Axial chord Reynolds number
λ = Light wavelength, eigenvalue
ϕ = Eigenfunction

References

[1] Ahuja, K. K., Whipkey, R. R., Jones, G. S., and Co, L., 1983, “Control of Turbulent Boundary Layer Flows by Sound,” AIAA 8th Aeroacoustics Conference, Atlanta, GA, Apr. 11–13.

[2] Zaman, K. B. M. Q., Bar-Sever, A., and Mangalam, S. M., 1987, “Effect of Acoustic Excitation on the Flow Over a Low-Re Airfoil,” J. Fluid Mech., **182**(1), pp. 127–148.

[3] Ahuja, K. K., and Burrin, R. H., 1984, “Control of Turbulent Boundary Layer Flows by Sound,” AIAA 9th Aeroacoustics Conference, Williamsburg, VA, Oct. 10-15, pp. 2298–2312.

[4] Zaman, K. B. M. Q., and McKinzie, D. J., 1991, “Control of Laminar Separation Over Airfoils by Acoustic Excitation,” AIAA J., **29**(7), pp. 1075–1083.

[5] Greenblatt, D., and Wygnanski, I. J., 2000, “Control of Flow Separation by Periodic Excitation,” Prog. Aerosp. Sci., **36**(7), pp. 487–545.

[6] Bernardini, C., Benton, S. I., and Bons, J. P., 2013, “The Effect of Acoustic Excitation on Boundary Layer Separation of a Highly Loaded LPT Blade,” ASME J. Turbomach., **135**(3), p. 051001.

[7] Pröbsting, S., and Yarusevych, S., 2021, “Airfoil Flow Receptivity to Simulated Tonal Noise Emissions,” Phys. Fluids, **33**(4), pp. 1–16.

[8] Arbey, H., and Bataille, J., 1983, “Noise Generated by Airfoil Profiles Placed in a Uniform Laminar Flow,” J. Fluid Mech., **134**, pp. 33–47.

[9] Pröbsting, S., and Yarusevych, S., 2015, “Laminar Separation Bubble Development on an Airfoil Emitting Tonal Noise,” J. Fluid Mech., **780**, pp. 167–191.

[10] Goldstein, M. E., Sockol, P. M., and Sanz J., 1983, “The Evolution of Tollmien—Schlichting Waves Near a Leading Edge. Part 2. Numerical Determination of Amplitudes,” J. Fluid Mech., **129**, pp. 443–453.

[11] Lam, S. H., and Rott, N., 1993, “Eigen-Functions of Linearized Unsteady Boundary Layer Equations,” ASME J. Fluids Eng., **115**(4), pp. 597–602.

[12] Goldstein, M. E., 1985, “Scattering of Acoustic Waves Into Tollmien-Schlichting Waves by Small Streamwise Variations in Surface Geometry,” J. Fluid Mech., **154**, pp. 509–529.

[13] Celik, A., Mitra, A., Agarwal, T., Clark, J., Jacobi, I., and Cukurel, B., 2024, “Exploring Physics of Acoustic Flow Control Over Airfoils Toward Potential Application to High Work and Lift Turbines,” ASME J. Turbomach., **146**(3), p. 031001.

[14] Tam, C. K. W., 1981, “The Excitation of Tollmien-Schlichting Waves in Low Subsonic Boundary Layers by Free-Stream Sound Waves,” J. Fluid Mech., **109**, pp. 483–501.

[15] Lord, W. K., MacMartin, D. G., and Tillman, G., 2000, “Flow Control Opportunities in Gas Turbine Engines,” Fluids 2000 Conference and Exhibit, Denver, CO, June 19-22, p. 2234.

[16] Miao, X., Zhang, Q., Wang, L., Jiang, H., and Qi, H., 2015, “Application of Riblets on Turbine Blade Endwall Secondary Flow Control,” J. Propul. Power, **31**(6), pp. 1578–1585.

[17] Sondergaard, R., Rivir, R., Bons, J., and Yurchenko, N., 2004, “Control of Separation in Turbine Boundary Layers,” Second AIAA Flow Control Conference, Portland, OR, June 28–July 1, p. 2201.

[18] Abuaf, N., Bunker, R. S., and Lee, C. P., 1998, “Effects of Surface Roughness on Heat Transfer and Aerodynamic Performance of Turbine Airfoils,” Proceedings of the ASME Turbo Expo, Stockholm, Sweden, June 2–5, pp. 522–529.

[19] Mulleners, K., Gilge, P., and Hohenstein, S., 2014, “Impact of Surface Roughness on the Turbulent Wake Flow of a Turbine Blade,” J. Aerodyn., **2014**, pp. 1–9.

[20] Genç, M. S., Koca, K., and Açikel, H. H., 2019, “Investigation of Pre-Stall Flow Control on Wind Turbine Blade Airfoil Using Roughness Element,” Energy, **176**, pp. 320–334.

[21] Glezer, A., 1997, “Shear Flow Control Using Synthetic Jet Fluidic Actuator Technology,” AFOSR Contractor’s Meeting on Turbulence and Internal Flows, Atlanta, GA, pp. 147–213.

[22] Amitay, M., Kibens, V., Parekh, D., and Glezer, A., 1999, “The Dynamics of Flow Reattachment Over a Thick Airfoil Controlled by Synthetic Jet Actuators,” 37th Aerospace Sciences Meeting and Exhibit, Reno, NV, Jan. 2–5, p. 1001.

[23] McCormick, D. C., 2000, “Boundary Layer Separation Control With Directed Synthetic Jets,” 38th Aerospace Sciences Meeting and Exhibit, Reno, NV, Jan. 10–13, p. 519.

[24] Redinioits, O. K., Wilson, L. N., Lagoudas, D. C., and Khan, M. M., 2002, “Development of a Shape-Memory-Alloy Actuated Biomimetic Hydrofoil,” J. Intell. Mater. Syst. Struct., **13**(1), pp. 35–49.

[25] Huang, J., Corke, T. C., and Thomas, F. O., 2006, “Plasma Actuators for Separation Control of Low-Pressure Turbine Blades,” AIAA J., **44**(1), pp. 51–57.

[26] Tyler, J. M., and Sofrin, T. G., 1962, “Axial Flow Compressor Noise Studies,” SAE Tech. Pap., p. 24. 10.4271/620532.

[27] Clark, J. P., Paniagua, G., and Cukurel, B., 2024, “On the Development of High-Lift, High-Work Low-Pressure Turbines,” ASME J. Turbomach., **146**(12), p. 121011.

[28] Praisner, T. J., and Clark, J. P., 2007, “Predicting Transition in Turbomachinery—Part I: A Review and New Model Development,” ASME J. Turbomach., **129**(1), pp. 1–13.

[29] Clark, J. P., 2022, “An Alternate Means to Form Non-Dimensional Products in Dimensional Analysis,” Proceedings of ASME Turbo Expo, Rotterdam, Netherlands, June 13–17, p. V005T08A003.

[30] Sauder, R. R., Wolff, M., Savela, G. E., Norris, G. B., Lethander, A. T., Posada, N. A., and Clark, J. P., 2024, “Experimental Evaluation of High Lift, High Work LPT Blades in a Transonic Cascade,” Proceedings of ASME Turbo Expo, London, UK, June 24–28, Vol. 88063, p. V12BT30A020.

[31] Ni, R. H., Humber, W., Ni, M., Capece, V. R., Ooten, M., and Clark, J., 2016, “Aerodynamic Damping Predictions for Oscillating Airfoils in Cascades Using Moving Meshes,” Proceedings of ASME Turbo Expo, Seoul, South Korea, June 13–17, Vol. 49842, p. V07BT34A012.

[32] Yakirevich, E., Miezner, R., Leizeronok, B., and Cukurel, B., 2018, “Continuous Closed-Loop Transonic Linear Cascade for Aerothermal Performance Studies in Microturbomachinery,” ASME J. Eng. Gas Turbines Power, **140**(1), p. 012301.

[33] Hirsch, C., 1993, “Advanced Methods for Cascade Testing,” NASA STI/Recon Technical Report , **94**(15119).

[34] Chue, S. H., 1975, “Pressure Probes for Fluid Measurement,” Prog. Aerosp. Sci., **16**(2), pp. 147–223.

[35] Settles, G. S., 2001, *Schlieren Und Shadowgraph Techniques: Visualizing Phenomena in Transparent Media—Experimental Fluid Mechanics*.

[36] Hargather, M. J., and Settles, G. S., 2012, “A Comparison of Three Quantitative Schlieren Techniques,” Opt. Lasers Eng., **50**(1), pp. 8–17. . Elsevier.

[37] Moise, P., Zauner, M., and Sandham, N. D., 2022, “Large-Eddy Simulations and Modal Reconstruction of Laminar Transonic Buffet,” J. Fluid Mech., **944**, pp. 1–48.

[38] Moise, P., Zauner, M., Sandham, N. D., Timme, S., and He, W., 2023, “Transonic Buffet Characteristics Under Conditions of Free and Forced Transition,” AIAA J., **61**(3), pp. 1061–1076.

[39] Clemens, N. T., and Narayanaswamy, V., 2014, “Low-Frequency Unsteadiness of Shock Wave/Turbulent Boundary Layer Interactions,” Annu. Rev. Fluid Mech., **46**(1), pp. 469–492.

[40] Aniffa, S. M., and Mandal, A. C., 2023, “Experiments on the Low-Frequency Oscillation of a Separated Shear Layer,” Phys. Rev. Fluids, **8**(2).

[41] Towne, A., Schmidt, O. T., and Colonius, T., 2018, “Spectral Proper Orthogonal Decomposition and Its Relationship to Dynamic Mode Decomposition and Resolvent Analysis,” J. Fluid Mech., **847**, pp. 821–867.

[42] Schmidt, O. T., and Colonius, T., 2020, “Guide to Spectral Proper Orthogonal Decomposition,” AIAA J., **58**(3), pp. 1023–1033.

[43] Sieber, M., Paschereit, C. O., and Oberleithner, K., 2016, “Spectral Proper Orthogonal Decomposition,” J. Fluid Mech., **792**, pp. 798–828.

[44] Schmidt, O. T., Towne, A., Rigas, G., Colonius, T., and Brès, G. A., 2018, “Spectral Analysis of Jet Turbulence,” J. Fluid Mech., **855**, pp. 953–982.

[45] Goldstein, M. E., and Hultgren, L. S., 1987, “A Note on the Generation of Tollmien-Schlichting Waves by Sudden Surface-Curvature Change,” J. Fluid Mech., **181**, pp. 519–525.